The International Journal of Advanced Manufacturing Technology (2026) 146:2199–2213
https://doi.org/10.1007/s00170-026-18913-w

ORIGINAL ARTICLE

Automated detection of edge trimming-induced delamination in GFRPs using SIFT-based image registration and differencing

Tamás Lukács[1] · Norbert Geier[1]

Received: 10 April 2026 / Accepted: 6 August 2026 / Published online: 12 August 2026

Abstract

Fibre-reinforced polymer (FRP) composites are increasingly used in aerospace and automotive applications due to their high strength and corrosion resistance, but their abrasive, heterogeneous structure makes post-processing difficult. A major machining defect is edge trimming-induced delamination, which affects both appearance and structural integrity. Existing measurement methods are often manual, subjective, and not fully reproducible. This study proposes an automated, reproducible method for measuring delamination using SIFT-based image registration and image differencing. The approach compares "before" and "after" images of FRP specimens, aligns them with the SIFT algorithm, and detects damage through pixel intensity changes. Validation was performed on glass fibre reinforced polymer (GFRP) composite specimens machined with a Ø10 mm FRAISA compression end mill and imaged using a telecentric Mitutoyo QIA505 digital microscope. Results were compared with semi-manual measurements. The proposed method showed excellent performance, with an accuracy of 0.998 ± 0.001, precision of 0.763 ± 0.109, and recall of 0.858 ± 0.094. Its speed and objectivity make it suitable for industrial quality control and large-scale composite engineering studies.

Keywords Composites · Machining · Delamination · Optical microscopy · DIP · GFRP

Nomenclature

Variables and parameters

$\boldsymbol{A}$	Matrix of the "before" image (1)
a_{ij}	Elements of matrix $\boldsymbol{A}$ (1)
A_{CCn}	Area of a specific connected component (px)
A_{min}	Minimum area threshold for noise filtering (px)
$\boldsymbol{B}$	Matrix of the "after" image (1)
b_{ij}	Elements of matrix $\boldsymbol{B}$ (1)
$\boldsymbol{B'}$	Matrix of the aligned "after" image (1)
b'_{ij}	Elements of matrix $\boldsymbol{B'}$ (1)
$\boldsymbol{C}$	Matrix of the difference image (1)
c_{ij}	Elements of matrix $\mathbf{C}$ (1)
$\boldsymbol{C'}$	Matrix of the horizontally aligned difference image (1)
c'_{ij}	Elements of matrix $\boldsymbol{C'}$ (1)
$\boldsymbol{D}$	Matrix of the edge-based segmented image (1)
d_{ij}	Matrix of the edge-based segmented image (1)
$\boldsymbol{E}$	Matrix of the area-based noise filtered image (1)
e_{ij}	Elements of matrix $\boldsymbol{E}$ (1)
fn	False negative values (1)
fp	False positive values (1)
i_{edge}	Row index of the machined edge (1)
L	Length of the examined edge (px)
S	Safety distance for thresholding (px)
S_d	Total delaminated area (px)
tn	True negative values (1)
tp	True positive values (1)
V_{max}	Maximum delamination depth (px)
$V_{max,exp}$	Expected maximum delamination depth (px)

Abbreviations

CC	Connected Component
CFRP	Carbon Fibre Reinforced Polymer
CT	Computed Tomography
FRP	Fibre Reinforced Polymer
GFRP	Glass Fibre Reinforced Polymer
MAE	Mean Absolute Error

✉ Norbert Geier
geier.norbert@gpk.bme.hu

[1] Department of Manufacturing Science and Engineering, Faculty of Mechanical Engineering, Budapest University of Technology and Economics, Műegyetem rkp. 3, Budapest H-1111, Hungary

PCC	Pearson Correlation Coefficient
RMSE	Root Mean Square Error
SD	Standard Deviation
SIFT	Scale-Invariant Feature Transform
UD-GFRP	Unidirectional Glass Fibre Reinforced Polymer

1 Introduction

Fibre-reinforced polymer (FRP) composites are essential materials in modern engineering, with their applications becoming widespread across numerous industrial fields, including aerospace, marine, robotics, energy, and beyond [1–4]. Their popularity is primarily driven by their high specific strength, excellent dimensional stability, and superior fatigue properties [5–7]. Furthermore, these materials are generally characterised by excellent corrosion resistance, which provides additional advantages and further expands their fields of application. Moreover, FRPs are highly customizable to meet specific requirements through the selection of reinforcement and matrix materials, the type of reinforcement (woven or non-woven continuous or chopped fibres), the stacking sequence (unidirectional or multidirectional), mixing ratios, and combinations with other materials (e.g., sandwich structures).

In recent decades, composite manufacturing technologies have also reached a high level of sophistication, enabling the production of parts with highly complex geometries, sometimes even in a single operation [8]. Nevertheless, in most cases, post-processing is required to achieve the final product [9]. This is typically necessary to remove excess material generated during production and to ensure the strict form, position, and dimensional tolerances required for assembly. These post-processing tasks are most frequently performed using mechanical machining processes, typically involving the machining of edges, slots, pockets, and holes. Thus, machining FRP composites is often unavoidable.

However, due to the anisotropic and inhomogeneous properties, as well as the typically abrasive nature of the reinforcing fibres, the chip formation mechanisms and the loads acting on the tool differ significantly from those observed in metals [10]. During the machining of FRP composites, several geometric defects may occur, such as machining-induced burrs [11], delamination [12], fibre pull-out [13], microcracking [14], and matrix smearing [15]. Among the potential defects, delamination is considered the most severe; beyond being an aesthetic flaw, it directly reduces the resultant strength of the FRP component, potentially leading to unexpected, premature failure [16]. Therefore, it is critical to minimise the extent and likelihood of delamination caused by machining.

To minimise machining-induced delamination, three fundamental research directions can be distinguished: (i) optimisation and control of process parameters [17, 18], (ii) development of toolpath strategies [19, 20], and (iii) special geometric design of tools and the application of coatings [21]. In the edge trimming of fibre-reinforced polymer composites, the fundamental influences of various machining parameters on delamination are already well-documented in the literature. For instance, the tool geometry, particularly the helix angle, plays a critical role, as the axial cutting force component is primarily responsible for machining-induced peel-up and push-out delamination [22, 23]. Therefore, tools with a zero-degree helix angle or compression end mills are frequently recommended to minimise and control these forces. Furthermore, process parameters such as feed rate and cutting speed significantly affect delamination; generally, a larger feed rate increases cutting forces and the probability of defect formation, whereas higher cutting speeds can decrease the delamination depth [24]. The fibre cutting angle (θ) also dictates the extent of the damage, with the range of $90° < \theta < 180°$ being particularly unfavourable and prone to significant delamination generation [25]. Additionally, the proper selection of the radial depth of cut and employing a down-milling strategy are recognised practices for achieving high-quality machined edge [26]. However, to reduce the extent of delamination through these efforts, it is essential to quantify delamination to track their effectiveness and rate the technologies under development.

In the present study, we focus on the detection of delamination caused by the edge trimming process (also known as side milling, edge routing or contour milling); therefore, the subsequent findings are primarily applicable to this specific process. Although the term "delamination" derives from the separation of layers, there is currently no consensus in the literature on its precise definition. For instance, some researchers classify uncut fibres and burrs as part of the delamination [27–29], while others refer to them as burrs [30–32]. In specific manufacturing contexts, the observed phenomena may not constitute interlaminar separation, but rather localised plastic deformation. This occurs when machining-induced stress concentrations exceed the material's elastic limit, leading to permanent microstructural changes — such as crazing and scission of polymer chains.

Despite these ambiguities, researchers strive to categorise delamination and introduce metrics to quantify its extent. In edge trimming, the most commonly used metrics are based on the area of surface damage (S_d) – hereafter referred to as the total delaminated area – and the maximum delamination depth measured perpendicular to the machined edge (V_{max}) [33–37]. To ensure that the results of different experiments are comparable, these aforementioned geometric characteristics can be normalised to a specific length. In the case of V_{max}, this means that the maximum delamination depth must be detected on sections of the same length, while in the case of S_d, the values can be determined over any chosen section, as long as the results are scaled to the length of the analysed section (S_d / L) [27].

The detection and measurement of machining-induced delamination are typically performed using digital image processing, for which the necessary images are obtained through various imaging techniques. Most frequently, images are captured using optical microscopy; however, other imaging methods such as Computed Tomography (CT) and ultrasound-based technologies are also employed. For example, Khashaba [38] measured drilling-induced delamination using an AutoCAD-based image processing (ACIP) technique, in which the drilled holes were first digitised using a high-resolution flatbed scanner and the images were processed in graphical software to isolate the damaged region around each hole. The delamination extent was then quantified by determining the maximum concentric and eccentric diameters tangent to the delamination boundary and by calculating the delaminated area, from which several delamination factors were derived relative to the nominal hole diameter. Nagarajan et al. [1] proposed an improved methodology for quantifying drilling-induced delamination in composite laminates by introducing a refined delamination factor derived using Buckingham's π-theorem. Instead of relying solely on the maximum delamination diameter, the method incorporates the delaminated area obtained through digital image analysis, providing a more representative characterisation of damage around drilled holes. Experimental results on glass fibre reinforced composites demonstrate that the proposed factor offers a more reliable evaluation of drilling damage and can support the optimisation of machining parameters. Lukács et al. [12] introduced an image differencing method for GFRP laminates by comparing images before and after drilling to isolate true delamination from other surface anomalies; their automated results closely matched conventional manual optical measurements. Maghami et al. [39] demonstrated a machine learning approach by fusing multi-angle illumination images and training a U-Net convolutional network to automatically segment drilled-hole images and detect damage; their model could infer hole profiles and delaminated areas directly from raw images, enabling real-time computation of the delamination factor with only about 5.4% error.

While numerous image processing methods have been introduced for measuring machining-induced delamination, these are primarily suited for drilling-induced delamination and cannot be directly adapted for edge trimming-induced delamination. In addition, these approaches are neither fully automated nor entirely reproducible, and also generally lack the capability to firmly distinguish between edge trimming-induced damage and other surface inconsistencies (e.g., dust, remaining marker lines, cracks and cavities). One of the best current methods is developed by Wang et al. [40]. They captured images of the workpiece surface not only after but also before edge trimming, subsequently detecting delamination areas actually caused by the edge trimming process based on the principle of image differencing, thereby excluding other surface discontinuities. However, they achieved this through a rather cumbersome procedure, utilising markers to align the "before" and "after" images and applying a colouring agent near the edge to be machined. The objective of the present study is to further exploit the potential of image differencing to develop a fully automated, reproducible, and accurate method for measuring edge trimming-induced delamination.

2 Description of the proposed delamination measurement method

The fundamental pillar of the proposed measurement method is that zones damaged during edge trimming "whiten" in FRP composites, a phenomenon attributed to changes in the composite's optical properties. Although two-dimensional microscopic images alone cannot determine whether this optical change stems exclusively from classical interlaminar separation or other damage mechanisms – such as localized plastic deformation, resin micro-cracking, or fibre-matrix debonding – the resulting light scattering remains clearly observable by the naked eye and detectable by computer vision systems (Fig. 1). In standard composite machining literature and quality control, all such visible machining-induced whitening is practically classified under the collective term of "delamination". Even if part of the whitening represents plastic deformation, resin micro-cracking, or fibre-matrix debonding rather than full layer separation, it signifies localized structural degradation and a critical zone for potential failure initiation, making its complete detection essential for evaluating machined edge integrity. Moreover, in an increasing number of high-end composite applications, surface aesthetics play a critical role. Consequently, even if this localized whitening does not severely compromise the component's mechanical performance or operational lifespan, it often constitutes an unacceptable visual defect that can lead to part rejection. However, the computer-vision-based exploitation of this promising "whitening" phenomenon remains challenging due to the highly textured surface

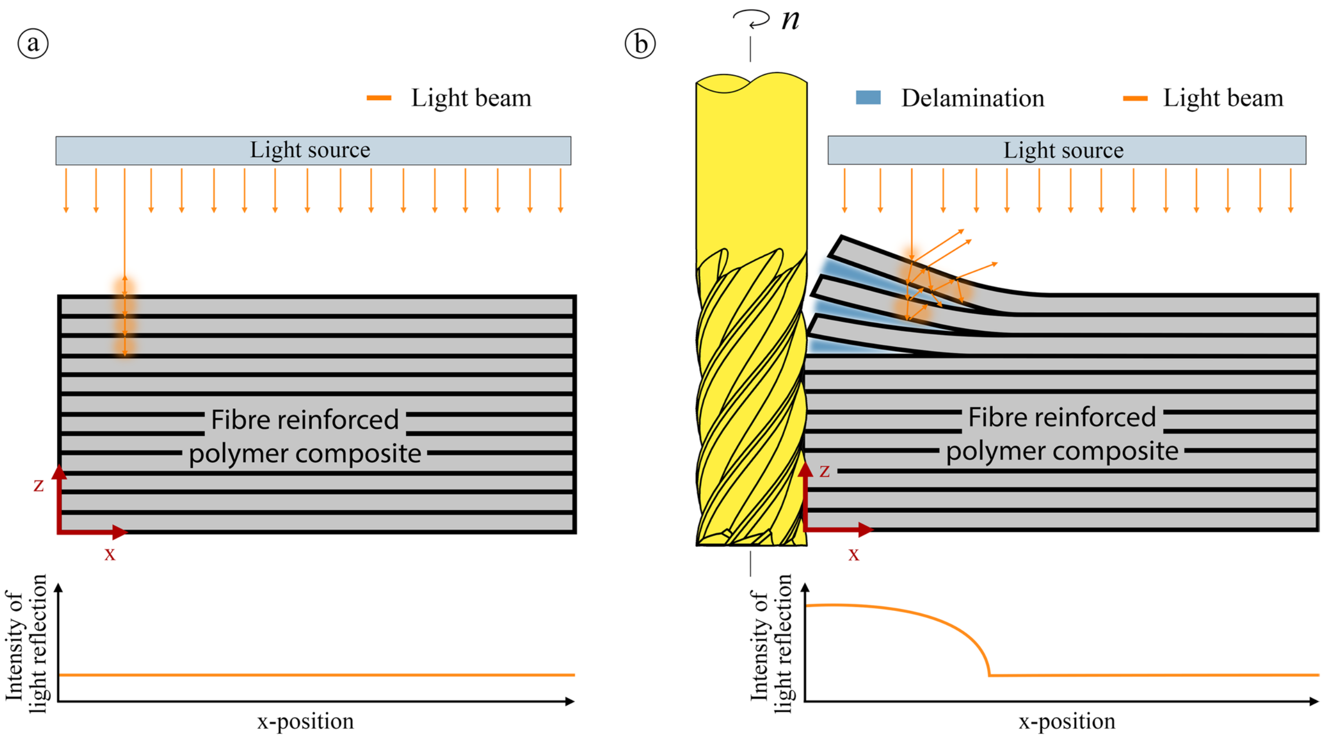

Fig. 1 Comparison of light reflection on (**a**) intact and (**b**) edge-trimmed composite surfaces

of FRP composites arising from the reinforcing and bundling fibres. This is particularly true for glass fibre reinforced polymer (GFRP) composites, as glass fibres near the surface reflect a large portion of the incident light, appearing as white areas in microscopic images – similar to the damaged areas induced by edge trimming – thereby making it difficult to distinguish between them.

To overcome this challenge, the principle of image differencing can be effectively applied, as it was proven in the case of circular delamination areas resulting from the drilling process [12]. According to this approach, images of the examined surface are captured both before and after edge trimming; by comparing these images, areas damaged exclusively during the edge trimming process can be detected. Utilising this principle, we have developed a novel measurement method capable of automated, rapid, and accurate measurement of edge trimming-induced delamination without the need for markers or other auxiliary tools. In this study, material fragments protruding beyond the machined edge – such as uncut fibres – were identified as burrs, while all other detected areas – except noise – were classified as delamination, as shown in Fig. 2.

Figure 3 illustrates the flowchart of the proposed edge trimming-induced delamination measurement method, which is detailed below, while the intermediate results of the method after its primary steps are shown in Fig. 4.

Fig. 2 Interpretation of delamination (red area), burr (blue area), and delamination measures of V_{max} and S_d

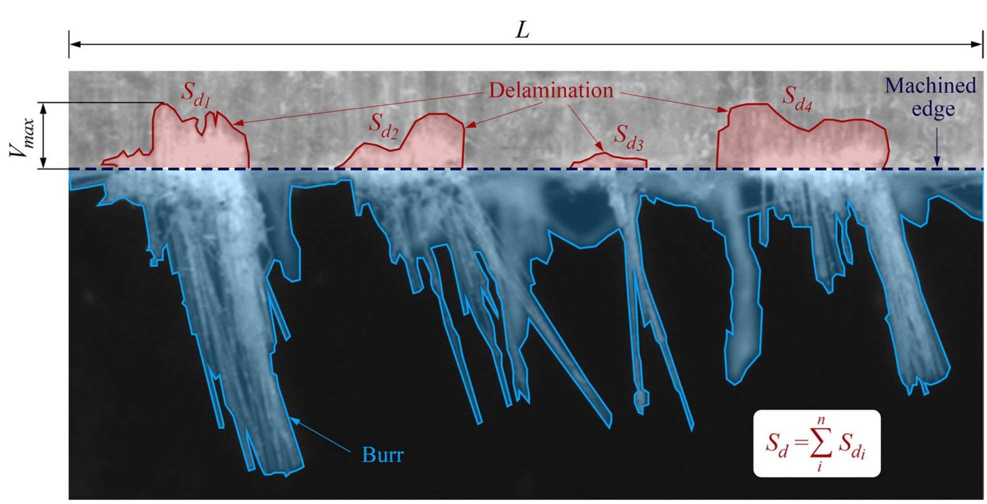

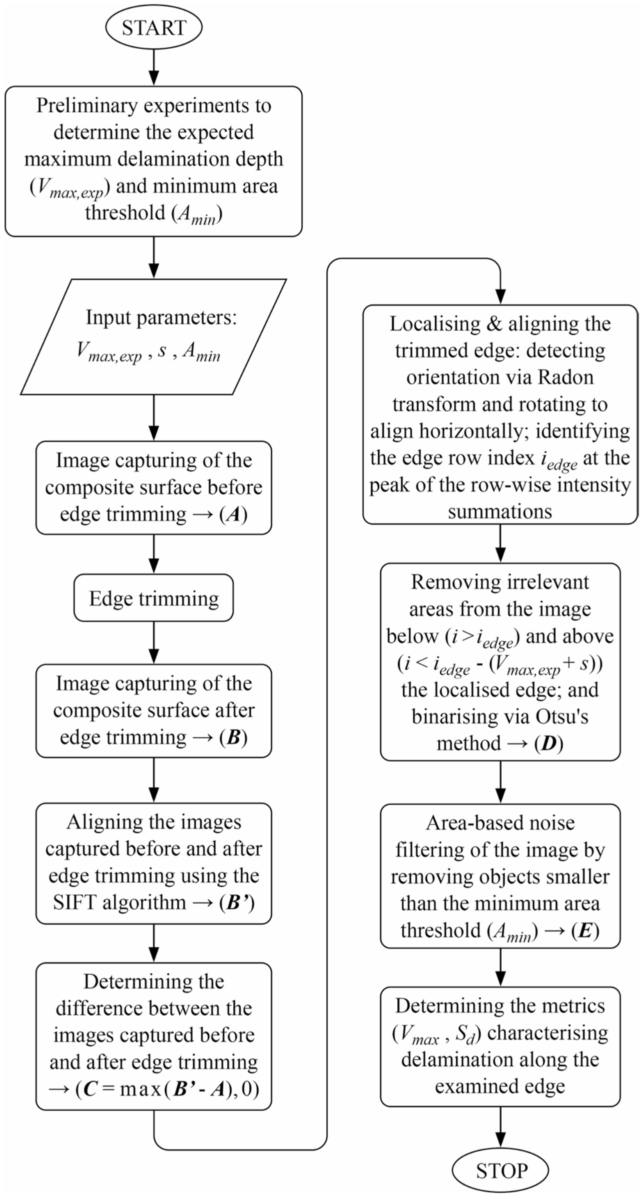

Fig. 3 Flowchart of the proposed edge trimming-induced delamination measurement method

(i) Capturing an image of the workpiece surface near the edge to be machined, preferably in greyscale mode; otherwise, convert it to greyscale so that each pixel contains only a single value (i.e., grey level). For image capturing, the use of a digital microscope is recommended, although it is not the only applicable device. It is crucial, however, to adjust the illumination to ensure that the image contains no saturated (overexposed) areas. It is recommended to capture the image with the edge to be machined positioned approximately horizontally. The pixels of the captured image are stored in matrix ***A***, and the elements of this matrix are denoted by a_{ij}, where i and j represent the rows and columns of the matrix, respectively. The matrix is formulated as expressed by Eq. (1). The resulting image of this step is illustrated in Fig. 4a.

$$A = \begin{pmatrix} a_{11} & \cdots & a_{1m} \\ \vdots & \ddots & \vdots \\ a_{n1} & \cdots & a_{nm} \end{pmatrix}; \; a_{ij} \in (0,\, 1 \ldots 255) \tag{1}$$

(ii) After edge trimming, a second image of the same workpiece surface must be captured under nominally identical imaging conditions. This requires not only maintaining the imaging device settings but also ensuring the workpiece is positioned as close as possible to its original orientation. Although the next step involves image registration to align the "before" and "after" images, maintaining a near-identical position is recommended to ensure consistent light reflection, thereby enhancing the overall accuracy of the method. The pixels of the captured image are stored in matrix ***B***, and the elements of this matrix are denoted by b_{ij}. The matrix is formulated analogously to Eq. (1). The resulting image of this step is illustrated in Fig. 4b.

(iii) Despite every effort to maintain consistent positioning during image acquisition (e.g., using a positioning device or fixture), capturing "before" and "after" images in the exact same orientation is technically unfeasible. Consequently, image alignment (i.e., image registration) is necessary. We employed the Scale-Invariant Feature Transform (SIFT) algorithm for computer-based alignment [41]. This method operates by detecting and describing local features (i.e., keypoints) that are robust to scaling, rotation, and changes in illumination, allowing for robust matching between the two images. In this study, the "after" images were aligned to their corresponding "before" images. The pixels of the aligned "after" image are stored in matrix ***B'***, and the elements of this matrix are denoted by b'_{ij}. The matrix is formulated analogously to Eq. (1). The resulting image of this step is illustrated in Fig. 4c.

(iv) Following the alignment process, the differences between the two images are identified by comparing their respective pixel intensities. Specifically, the "before" matrix (***A***) is subtracted from the aligned "after" matrix (***B'***). Depending on the data type of the matrices, this operation may result in negative values, particularly in areas where material has been removed. As these areas are irrelevant to the current analysis, the values of these elements are adjusted to zero

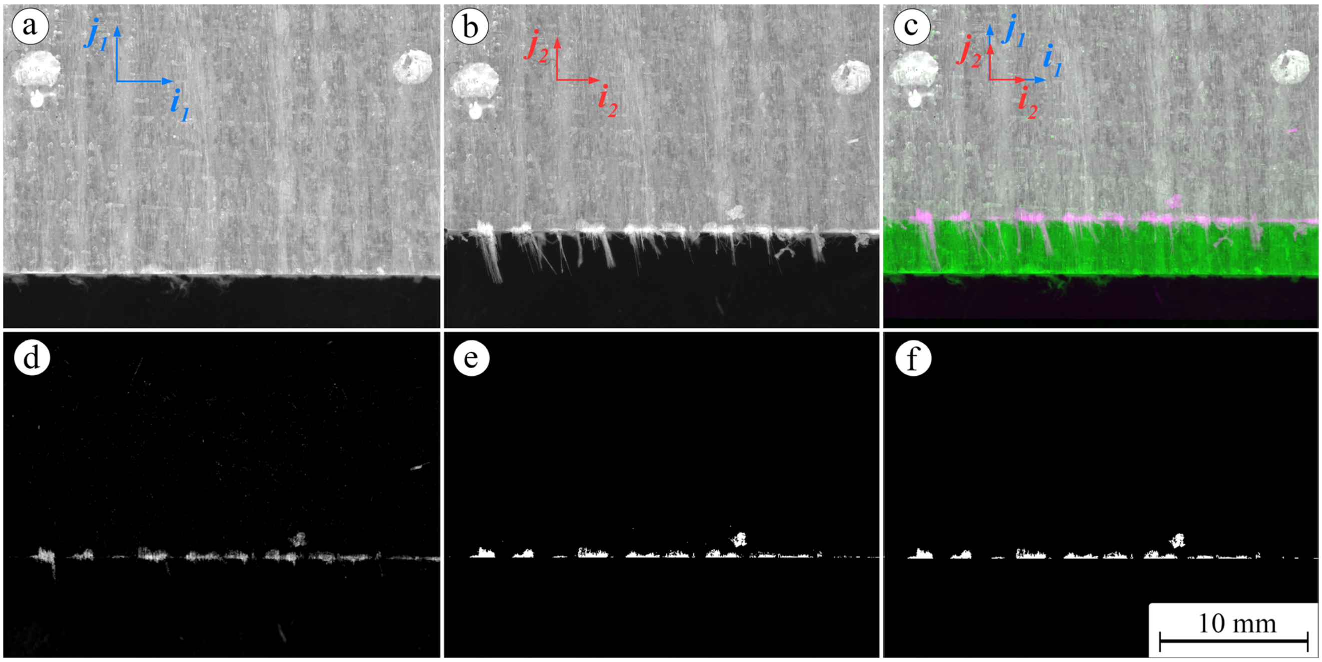

Fig. 4 Intermediate results of the proposed method: (**a**) image before edge trimming, (**b**) image after edge trimming, (**c**) registered image, (**d**) difference between aligned images, (**e**) edge-based segmented image, (**f**) area-based noise filtered image ready for delamination characterisation

(black). The resulting pixel values are stored in matrix ***C***, with elements denoted c_{ij}. The matrix is formulated as expressed by Eq. (2), where the max function is applied element-wise. The resulting image of this step is illustrated in Fig. 4d.

$$C = max(B^{'} - A,\ 0) \tag{2}$$

(v) This step involves the removal of irrelevant data, which includes artefacts beyond the machined edge (such as burrs and noise), as well as noisy regions located above the highest point of delamination (Vmax). To define these boundaries between relevant and irrelevant regions, the machined edge is first precisely localised and aligned horizontally.

To achieve this, we employed the Radon transform on the difference image (***C***) to detect the dominant linear feature corresponding to the machined edge. Since machining-induced delamination (and burrs) inherently initiates from the trimmed edge, the highest concentration of bright pixels is located along this line. Consequently, by calculating line integrals across different projection angles, the exact orientation of the machined edge can be identified by finding the specific linear trajectory along which the cumulative greyscale pixel intensity is maximised. It is recommended to use a constrained angular window (e.g., ± 10°) around the nominal edge angle to prevent orientation inversion and optimise computational efficiency. Based on the detected angle, the difference image is rotated around its centre to align the machined edge parallel to the horizontal axis. The pixels of this horizontally aligned difference image are stored in matrix ***C’***, and the elements of this matrix are denoted by c'_{ij}.

While the row index of the machined edge could theoretically be derived directly from the Radon transform, to ensure absolute accuracy after discrete image rotation, a refinement step is performed. Employing a principle analogous to the Radon transform, a row-wise summation of greyscale pixel intensities is calculated across the rotated matrix ***C’***, identifying the exact edge index, i_{edge}, at the row where this cumulative sum is maximised, as shown in Eq. (3).

$$i_{edge} = arg\ \underset{i}{max} \sum_{j} c'_{\ ij} \tag{3}$$

Once the location of the machined edge is established, all elements located below this specific row are set to zero (black). A similar procedure is applied to the region above the maximum delamination depth (V_{max}). For this step, an empirical threshold is required, which can be easily determined through preliminary experiments. This threshold is defined as the expected maximum delamination depth ($V_{max,\ exp}$) plus a safety distance (s); consequently, all matrix elements located beyond this distance above the detected edge are also adjusted to zero (black). In this study, $V_{max,\ exp}$ was set to 100 pixels. Finally, to prepare the image for the subsequent step, it is binarised using Otsu's method. The resulting pixel values are stored in matrix $\boldsymbol{D}$, with elements denoted d_{ij}. The matrix is formulated as expressed by Eq. (4). The resulting image of this step is illustrated in Fig. 4e.

$$d_{ij} = \begin{cases} c_{ij} & , \ i_{edge} - (V_{max,\ exp} + s) \leq i \leq i_{edge} \\ 0 & , \ otherwise \end{cases} \tag{4}$$

(vi) Despite the previous steps, small, disconnected pixel clusters (i.e., noise) may remain that do not represent actual delamination. Therefore, to further refine the results and eliminate residual noise, an area-based filtering operation is performed. In this process, connected components (CC) are identified, which are defined as discrete objects formed by groups of adjacent non-zero (non-black) pixels. The area of each such object is calculated based on its total pixel count. A minimum area threshold A_{min} is established to distinguish between relevant features and noise. In this study, A_{min} was set to 100 pixels; however, it should be noted that this threshold is highly dependent on the experimental conditions, particularly the image resolution. Any connected component (CC_n) with an area (A_{CCn}) smaller than A_{min} is considered noise; consequently, the values of the corresponding elements in matrix $\boldsymbol{D}$ are adjusted to zero (black). The resulting pixel values are stored in matrix $\boldsymbol{E}$, with elements denoted e_{ij}. The matrix is formulated as expressed by Eq. (5). This ensures that only significant delamination zones are preserved for the final calculations. The resulting image of this step is illustrated in Fig. 4f.

$$e_{ij} = \begin{cases} 0 & , \ (i,\ j) \in CC_n \ and \ A_{CC_n} < A_{min} \\ d_{ij} & , \ otherwise \end{cases} \tag{5}$$

(vii) Finally, the metrics quantifying edge trimming-induced delamination are determined. The maximum delamination depth (V_{max}) is calculated by identifying the first row in matrix $\boldsymbol{E}$ that contains at least one non-zero element; the index of this row is then subtracted from the previously established machined edge index i_{edge}, as shown in Eq. (6). Furthermore, the total delaminated area (S_d) is obtained by summing the values of all elements within matrix $\boldsymbol{E}$, as shown in Eq. (7).

$$V_{max} = i_{edge} - min\left\{ i \mid \sum_{j} e_{ij} > 0 \right\} \tag{6}$$

$$S_d = \sum e_{ij} \tag{7}$$

To confirm the stability of the proposed method, a parameter robustness study was conducted across all 14 specimens. The results demonstrate that above certain thresholds ($V_{max,\ exp}$ = 100 px and A_{min} = 75 px), the evaluated metrics (V_{max} and S_d) reach a stable plateau, becoming nearly constant and invariant to further parameter increases. Note that the safety distance s was not evaluated separately, as increasing $V_{max,\ exp}$ inherently achieves the exact same geometrical expansion of the region of interest ($V_{max,\ exp} + s$). These findings confirm that the proposed algorithm is highly robust and operates reliably without requiring specimen-specific parameter tuning.

3 Experimental setup

In this study, specimens of eight-layered unidirectional glass fibre-reinforced polymer (UD-GFRP) composites and nonwoven-mat glass fibre-reinforced polymer composites were used to validate the proposed method. The UD-GFRP specimens were fabricated through compression moulding and consisted of NOVIA unidirectional glass fabric (with a surface mass of 200 g/m^2) embedded in an epoxy matrix (composed of IPOX MR1010 resin and IPOX MH3124 hardener in a ratio of 100 : 33, respectively). The nonwoven-mat reinforced composites were fabricated similarly to the UD-GFRP but using a NOVIA nonwoven-mat glass with a surface mass of 225 g/m^2. The curing process for the laminated specimens involved exposure to a temperature of 80 °C and a pressure of 100 bar for a duration of 20 min. The thickness of the specimens was set to 3.5 mm. The edge trimming operations were performed on a Kondia B640 machining centre. The resulting chips were removed from the cutting zone using a NILFISK GB733 industrial vacuum cleaner. For the edge trimming, a Ø 10 mm FRAISA 20360.450 (coarse tooth) uncoated carbide compression end mill was used, as shown in Fig. 5b. The composite specimens were fixed between a lower and upper fixture plate as shown in Fig. 5a. The machining operations were carried out at a feed rate of 1760 mm/min and a cutting speed of 160 m/min, without the use of any coolant.

A telecentric Mitutoyo QIA505 digital microscope (operating in dome lighting mode at 76% of its maximum illuminating power of 3 W) was used to capture images of the specimens both before and after the edge trimming operations (Fig. 6). The microscope was set at a nominal magnification of 5x with a resolution of 1280 × 960 pixels. Subsequently, the microscopic images were assessed using two approaches: manual masking and the image processing method outlined in Sect. 2.

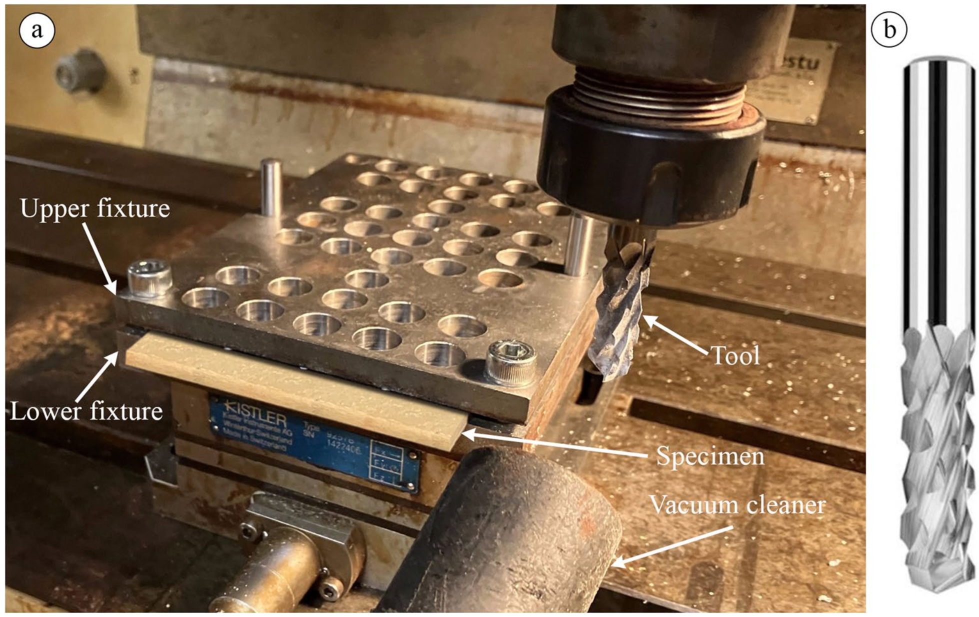

Fig. 5 Experimental setup: (**a**) edge trimming environment (**b**) uncoated carbide end mill

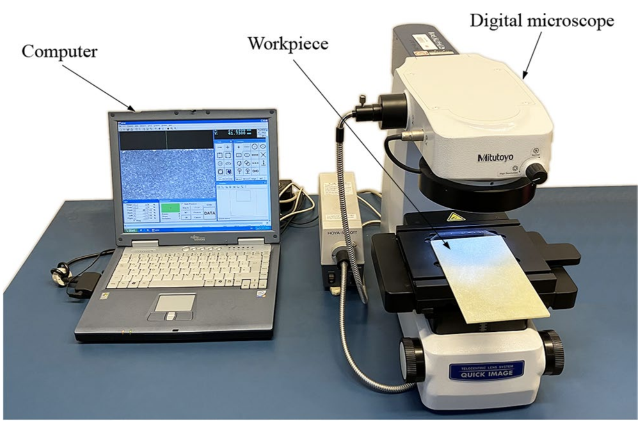

Fig. 6 Image capturing setup

4 Results and discussion

4.1 Results and validation

The proposed measurement method was validated by comparing its outputs against manual evaluations across 14 distinct GFRP specimens. In this validation process, the manual detection method was considered the reference (ground truth). Although the precision of the human eye is remarkable, the delineation of delaminated areas and the localisation of the machined edge during manual masking remain largely subjective; furthermore, as discussed in Sect. 1, edge-trimming induced delamination can be difficult to distinguish from other material discontinuities in certain cases, meaning that this method is also prone to errors. However, no better reliable methods exist that are generally accepted by the community. To clarify the proposed evaluation methodology, the performance metrics were calculated on a pixel-by-pixel basis. Consequently, they represent the evaluated area, and their fundamental unit is pixels (which corresponds to physical area). As conceptually illustrated in Fig. 7, these areas are determined by the spatial overlap between the manual reference mask (ground truth, solid line) and the output of the proposed method (predicted, dashed line). This relationship is visually mapped by highlighting *tp* true positives (the green overlapping area of correctly identified delamination), *fp* false positives (the blue area incorrectly identified as delamination), *fn* false negatives (the red area representing actual delamination that the proposed method failed to detect), and *tn* true negatives (the white background area of correctly identified intact regions). Finally, the visual comparisons in Fig. 8 demonstrate the practical performance of

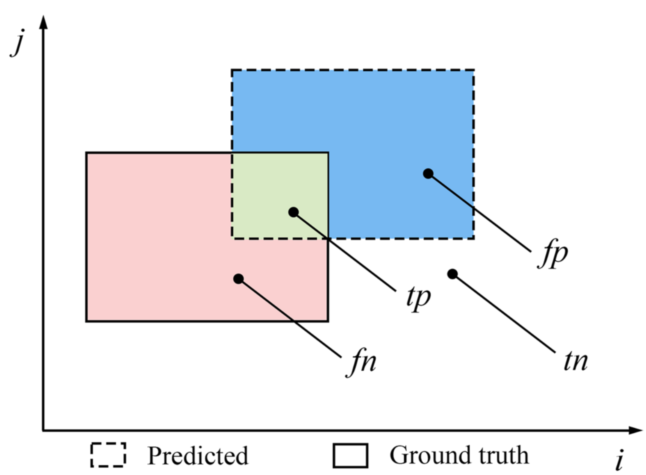

Fig. 7 Geometric interpretation of true positives (*tp*), false positives (*fp*), false negatives (*fn*), and true negatives (*tn*) for pixel-based classification

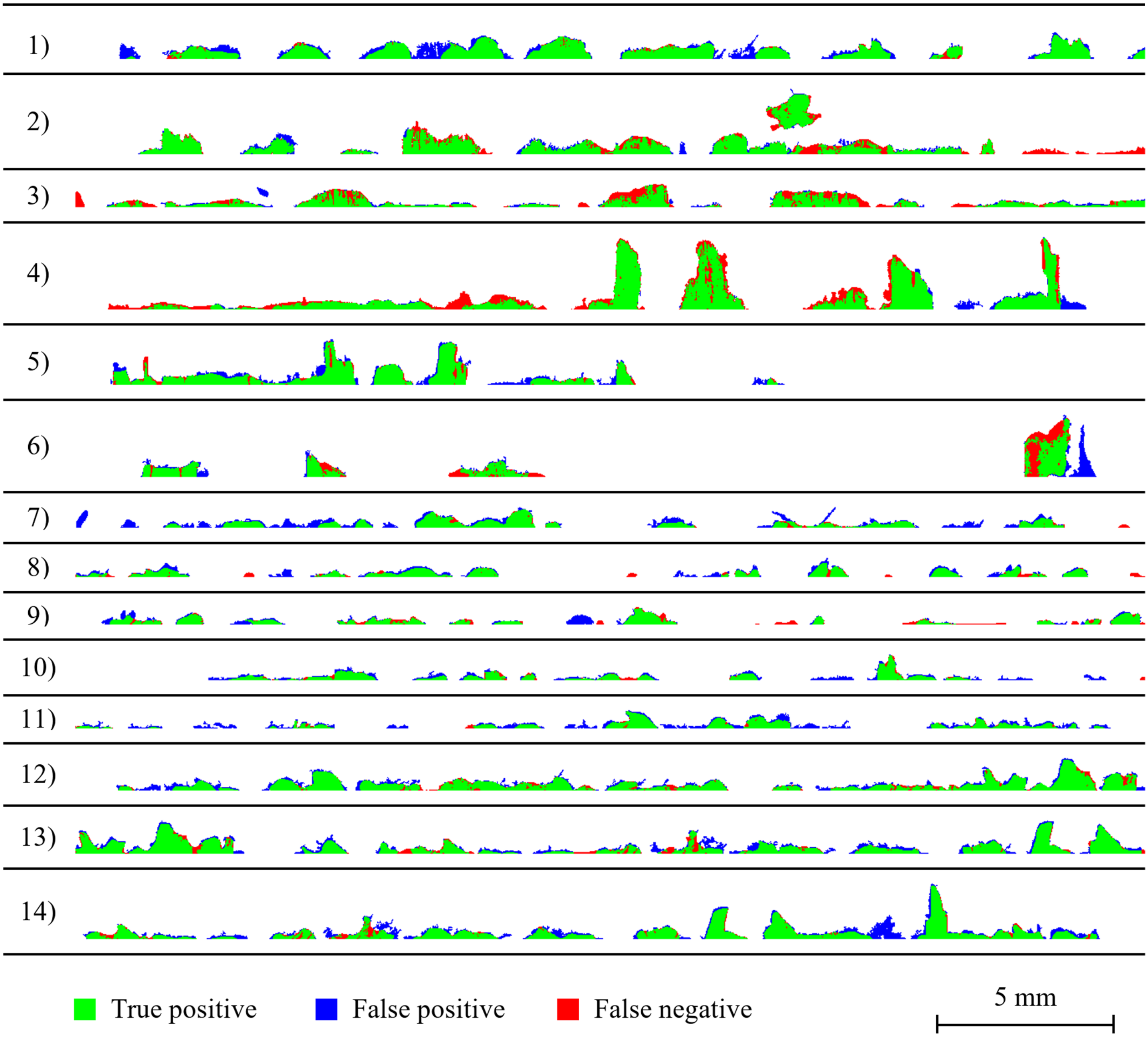

Fig. 8 Comparison of the proposed method against manual evaluation

the proposed method by mapping these exact, colour-coded areas onto the actual machined specimens.

Although the dominance of green (*tp*) and white (*tn*) colours suggests that the proposed method is excellent, a quantitative assessment was performed to evaluate the proposed method's effectiveness at the pixel level using numerical performance metrics. Figure 9 presents the confusion matrix for this pixel-level classification. The matrix was row-normalised, which is a critical step for this specific evaluation; since the intact composite surface (the background) constitutes the vast majority of the image pixels, calculating raw proportions over the entire image would heavily skew the results. Row normalisation ensures that the classification accuracy for both the delaminated (positive) and intact (negative) classes is represented proportionally to their actual occurrences, preventing the background from masking the true detection performance of the relatively small damaged regions.

The normalised confusion matrix reveals that the proposed method successfully identified 84.5% of the actual delaminated pixels, corresponding to the true positive rate. Consequently, the false negative rate was 15.5%, meaning this proportion of actual delamination was missed. This discrepancy is presumably largely caused by the fact that the manual measurement method, used as the reference, cannot be considered a perfect ground truth due to its

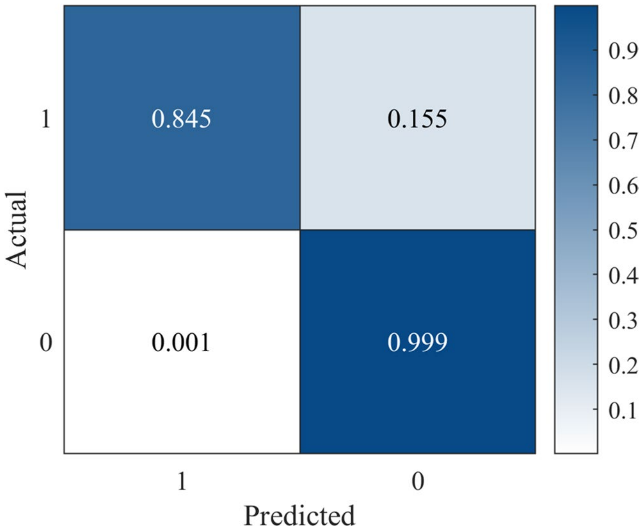

Fig. 9 Illustration of the performance of the proposed method using a normalised (row-wise) confusion matrix

inherent subjectivity. Furthermore, some relevant delaminated areas are also lost during the automated noise-filtering step. The method achieved an exceptional 99.9% true negative rate in correctly identifying intact regions, with a mere 0.1% false positive rate, demonstrating its robustness against false alarms.

To further detail the proposed method's reliability, Fig. 10 and Table 3 (in the appendices) summarise specific performance metrics evaluated across all GFRP specimens. *Precision*, which indicates the proportion of positively identified pixels that were actually delaminated (i.e., tp / (tp+fp)), yielded a mean value of 0.763 ± 0.109. This shows that when the proposed method detects delamination, it is generally correct, though minor false positive clusters occasionally occur. *Recall* (or sensitivity), represents the ratio of correctly predicted positive observations to all actual positives (i.e., tp / (tp+fn)), achieving a mean of 0.858 ± 0.094. This high value confirms the method's strong capability to capture the majority of the true delamination. The overall accuracy (*Accuracy* = (tp+tn) / (tp+tn+fp+fn)) of the model was near-perfect at 0.998 ± 0.001; however, this metric is heavily influenced by the overwhelmingly large, correctly classified background area. Finally, the Intersection over Union (*IoU*=tp / (tp+fp+fn)), a stringent metric that measures the spatial overlap between the predicted and ground-truth delamination areas, resulted in a mean score of 0.666 ± 0.072. This score is highly satisfactory for automated defect detection.

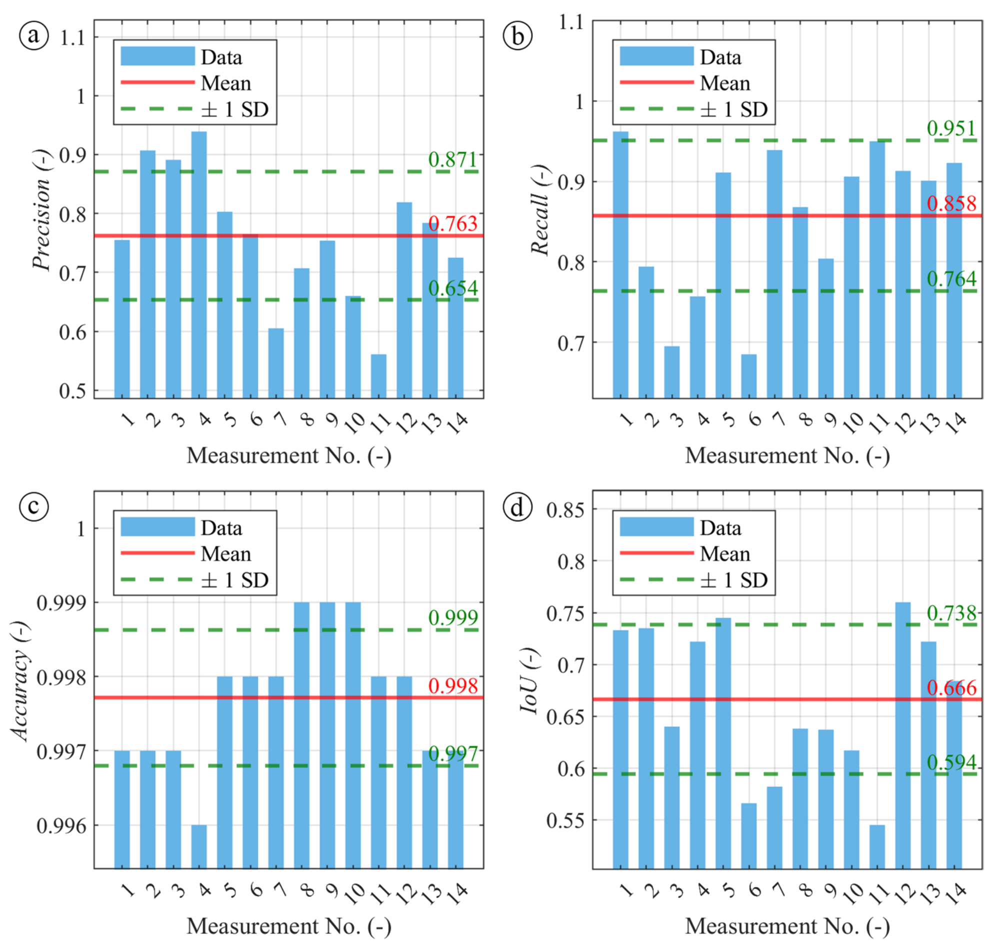

Fig. 10 Performance metrics of the proposed method: (**a**) *Precision*, (**b**) *Recall*, (**c**) *Accuracy*, and (**d**) *IoU*

In addition to the performance metrics, the proposed method was also evaluated based on the delamination factors: maximum delamination depth (V_{max}) and the total delaminated area (S_d). Values obtained via the manual and the proposed methods for both metrics were summarised (Table 1) and compared using Bland-Altman plots (Figs. 11 and 12) and correlation parameters (Table 2).

Figure 11 shows the Bland-Altman plot comparing the manually measured maximum delamination depth (V_{max}) values with those obtained with the proposed method. It reveals a mean difference (bias) of −2.29 pixels, indicating that the proposed method slightly overestimates the maximum delamination depth compared to the manual reference. Nearly all data points fall within the 95% limits of agreement (ranging from −6.73 to 2.16 pixels), with only one measurement (data point 2) falling just outside the lower boundary. This demonstrates high precision and consistent performance across the tested range. Furthermore, the correlation between manual and algorithmic (measured by the proposed method) measurements for V_{max} is exceptionally high, supported by a Pearson Correlation Coefficient (*PCC*) of 0.996 and a Spearman's ρ of 0.981. The Mean Absolute Error (*MAE*) for V_{max} is 2.571 pixels, while the Root Mean Square Error (*RMSE*) is 3.162 pixels, confirming the method's reliability for identifying the peak extent of the damage.

Figure 12 presents the Bland-Altman plot for the total delaminated area (S_d), illustrating the agreement between manual measurements and the proposed automated method. The mean difference (bias) for S_d measurement is −525 pixels. This negative bias suggests that, on average, the proposed method detects a slightly larger total delaminated area than the manual method. This also suggests that the

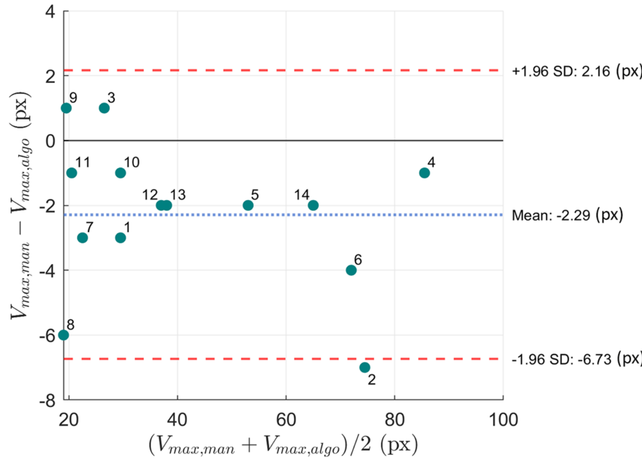

Fig. 11 Bland-Altman plot for the validation of maximum delamination depth (V_{max})

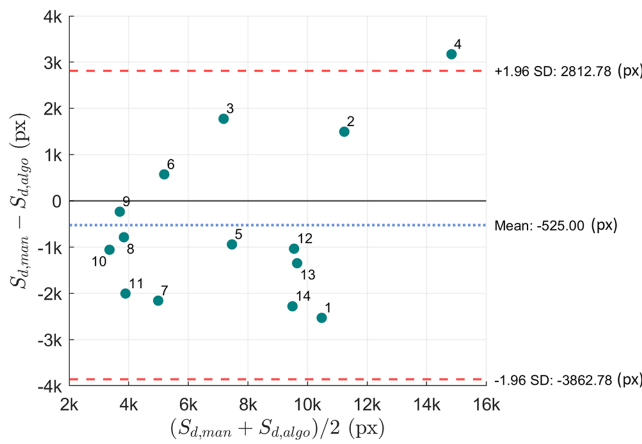

Fig. 12 Bland-Altman plot for the validation of total delaminated area (S_d)

Table 1 Delamination factors obtained through the manual (man) and proposed (algo) methods

No.	Manual method				Proposed method			
	$V_{max,\ man}$		$S_{d,\ man}$		$V_{max,\ algo}$		$S_{d,algo}$	
	(px)	(mm)	(px)	(mm^2)	(px)	(mm)	(px)	(mm^2)
1	28	0.66	9210	5.06	31	0.73	11,739	6.45
2	71	1.66	11,980	6.58	78	1.83	10,486	5.76
3	27	0.63	8070	4.43	26	0.61	6296	3.46
4	85	1.99	16,418	9.02	86	2.02	13,246	7.28
5	52	1.22	6994	3.84	54	1.27	7933	4.36
6	70	1.64	5475	3.01	74	1.73	4904	2.69
7	21	0.49	3908	2.15	24	0.56	6065	3.33
8	16	0.38	3444	1.89	22	0.52	4228	2.32
9	20	0.47	3579	1.97	19	0.45	3817	2.10
10	29	0.68	2826	1.55	30	0.70	3881	2.13
11	20	0.47	2888	1.59	21	0.49	4891	2.69
12	36	0.84	9031	4.96	38	0.89	10,063	5.53
13	37	0.87	8977	4.93	39	0.91	10,323	5.67
14	64	1.50	8355	4.59	66	1.55	10,633	5.84

Table 2 Correlation parameters between manual and algorithmic measures

Metric (-)	*PCC* (-)	Spearman's ρ (-)	*MAE* (px)	*RMSE* (px)
V_{max}	0.996	0.981	2.571	3.162
S_d	0.903	0.921	1526.571	1722.940

manual method presumably misses certain areas of delamination (typically those with lower contrast, making them difficult to detect with the naked eye but clearly identifiable via image differencing) that the proposed method successfully detects. The vast majority of the data points remain well within the ±1.96 Standard Deviation (SD) boundaries (ranging from −3862.78 to 2812.78 pixels), with only a single outlier (data point 4) exceeding the upper limit. The overall correlation for S_d remains strong, with a *PCC* of 0.903 and a Spearman's ρ of 0.921. The associated *MAE* is 1526.571 pixels, and the *RMSE* is 1722.940 pixels. Despite the presence of these variances, the results confirm that the automated method provides an objective, robust, and reproducible alternative for area quantification.

4.2 Discussion and outlooks

The results presented in the previous subsection demonstrate that the proposed image differencing measurement method provides a robust and automated alternative to existing delamination assessment techniques. Despite the inherent subjectivity and potential inaccuracies of the manual reference method used for comparison, the evaluated performance metrics indicate that the proposed method demonstrates highly satisfactory performance. In addition to the performance metrics, the exceptionally high correlation for the maximum delamination depth (V_{max}) ($PCC = 0.996$, Spearman's $\rho = 0.981$) and the minimal bias of −2.29 pixels indicate that the proposed method is highly reliable in identifying the peak extent of the damage, which is often the most critical parameter for structural integrity assessments. Regarding the measurement of the total delaminated area (S_d) the observed average bias of −525.00 pixels indicates that the proposed method, on average, identifies a slightly larger area as delamination compared to the manual evaluation. Although the area-based noise-filtering step may have a tendency to 'thin' the detected zones, this effect is more than compensated for by the fact that the proposed method successfully detects lower-contrast delaminated regions that the manual method presumably overlooks.

A significant advantage of this method, particularly for GFRP composites, is its ability to distinguish between surface discontinuities and actual machining-induced damage. By utilising the "before" image as a baseline, the method effectively filters out pre-existing inconsistencies that often lead to overestimation in traditional single-image processing techniques. Furthermore, the automation of the machined edge localisation (Step v)) and the area-based noise filtering (Step vi)) enables rapid processing of large datasets.

Considering that the core of the proposed method is built upon robust SIFT-based image alignment and image differencing, it holds strong potential for broader applicability. The inherent resilience of feature-based registration against minor scale and positional shifts suggests that the methodology could be implemented across various optical setups and inspection environments with straightforward calibration. This underlying versatility also indicates that the approach can be readily adapted to other materials, such as carbon fibre reinforced polymer (CFRP) composites, where the optical contrast between damaged and intact zones may differ, but the fundamental principle of image differencing remains valid.

In the broader context of manufacturing, the specific benefit of this paper lies in providing a robust, objective, and automated evaluation tool. While the fundamental influences of cutting parameters (e.g., feed rate, tool geometry) on delamination are already well-documented in the literature, measuring these defects remains a highly subjective and labour-intensive process. The proposed method bridges this critical research gap. By overcoming the limitations of manual evaluations, this automated visual identification eliminates human error and paves the way for standardised industrial quality control. Furthermore, it enables the generation of massive, reliable datasets required for tool-wear monitoring, AI-driven process optimization, and smart manufacturing systems.

Future research could focus on integrating this method into real-time monitoring and in-situ inspection systems within machining environments. For instance, by mounting two properly calibrated digital microscopes directly onto the spindle housing – one positioned ahead of the cutting tool to capture the "before" images, and one behind to capture the "after" images – immediate, real-time feedback on delamination levels could be achieved. Additionally, this hardware-based alignment could entirely eliminate the need for the computational image registration step, making the process significantly faster and computationally lighter, thereby outperforming previous measurement methods. This real-time direct data could then signal the necessity for timely interventions, such as replacing excessively worn tools when the induced delamination exceeds the acceptable limit.

5 Conclusions

Based on the research and experimental results presented in this study, the following conclusions can be drawn:

- A novel, automated delamination measurement method based on image differencing was successfully developed for edge trimming of GFRP composites. By employing the Scale-Invariant Feature Transform (SIFT) algorithm for robust feature matching and image registration, the method entirely eliminates the need for markers or other auxiliary tools. By utilising and comparing the "before" and "after" images, the proposed method ensures that exclusively the edge trimming-induced delamination is detected, effectively filtering out any pre-existing material defects or surface inconsistencies. This approach significantly enhances the reproducibility and objectivity of the evaluation process, providing a reliable alternative to existing delamination assessment techniques.
- The pixel-level performance metrics demonstrate the reliability of the proposed method. With a high average recall of 0.858, the method demonstrates a strong capability to capture the vast majority of true delamination, thereby minimising the risk of overlooking critical structural damage. The near-perfect overall accuracy (0.998) highlights its exceptional true negative rate and robustness against false alarms across the extensive intact background. Additionally, the precision (0.762) and Intersection over Union (0.666) scores confirm a highly satisfactory spatial overlap with the manual reference, ensuring a consistent and objective evaluation of the damaged regions.
- The proposed method shows exceptional accuracy in determining the maximum delamination depth (V_{max}), evidenced by a remarkably low mean difference (bias) of only −2.29 pixels. This minimal bias, combined with a Pearson Correlation Coefficient (*PCC*) of 0.996 and a Spearman's ρ of 0.981 compared to manual measurements, confirms that the automated detection is nearly perfectly aligned with the reference manual measurements. This makes the proposed method highly reliable for structural integrity evaluations where peak damage is the critical factor.
- While the measurement of the total delaminated area (S_d) exhibited a slight overestimating bias of −525 pixels compared to manual evaluation, it maintained a strong statistical correlation with a *PCC* of 0.903 and a Spearman's ρ of 0.921. This discrepancy is presumably largely caused by the fact that the manual measurement method, used as the reference, cannot be considered a perfect ground truth due to its inherent subjectivity. Furthermore, some genuinely relevant delaminated areas are also lost during the method's automated noise-filtering step.
- The method's speed and lack of human subjectivity make it suitable for industrial quality control and large-scale parametric studies in composite machining. Furthermore, the underlying principle is versatile and can be adapted to other composites, such as CFRP composites.

Appendices

Table 3 Performance metrics of the proposed method

No.	*Precision* (-)	*Recall* (-)	*Accuracy* (-)	*IoU* (-)
1	0.755	0.962	0.997	0.733
2	0.907	0.794	0.997	0.735
3	0.891	0.695	0.997	0.640
4	0.939	0.757	0.996	0.722
5	0.803	0.911	0.998	0.745
6	0.765	0.685	0.998	0.566
7	0.605	0.939	0.998	0.582
8	0.707	0.868	0.999	0.638
9	0.754	0.804	0.999	0.637
10	0.660	0.906	0.999	0.617
11	0.561	0.950	0.998	0.545
12	0.819	0.913	0.998	0.760
13	0.784	0.901	0.997	0.722
14	0.725	0.923	0.997	0.684
Mean ± SD	0.763 ± 0.109	0.858 ± 0.094	0.998 ± 0.001	0.666 ± 0.072

Acknowledgements The edge trimming-induced delamination measurement method presented in this study is the subject of a pending patent (Application No. P2400285). This research was partly supported by the Doctoral Excellence Fellowship Programme (DKÖP), funded by the National Research, Development and Innovation Fund of the Ministry of Culture and Innovation and the Budapest University of Technology and Economics (BME), under a grant agreement with the National Research, Development and Innovation Office; and partly supported by the János Bolyai Research Scholarship of the Hungarian Academy of Sciences No. BO/00508/22/6.

Authors' contributions Tamás Lukács: Conceptualization, Investigation, Methodology, Formal analysis, Visualization, Writing - Original Draft; Norbert Geier: Conceptualization, Methodology, Investigation, Writing - Original Draft.

Funding Open access funding provided by Budapest University of Technology and Economics. Not applicable.

Data Availability The data that support the findings of this study are available from the corresponding author, upon reasonable request.

Code Availability Not applicable.

Declarations

Ethics approval Not applicable.

Consent to participate Not applicable.

Consent for publication Not applicable.

Conflicts of interest/Competing interests Not applicable.

Declaration of generative AI and AI-assisted technologies in the writing process During the preparation of this work, the authors used ChatGPT and Gemini in order to improve the English text. After using this tool, the authors reviewed and edited the content as needed and take full responsibility for the content of the publication.

References

1. Nagarajan VA, Selwin Rajadurai J, Annil kumar T (2012) A digital image analysis to evaluate delamination factor for wind turbine composite laminate blade. Compos Part B: Eng 43:3153–3159. https://doi.org/10.1016/j.compositesb.2012.04.013
2. Atescan-Yuksek Y, Mills A, Ayre D, Koziol K, Salonitis K (2024) Comparative life cycle assessment of aluminium and CFRP composites: the case of aerospace manufacturing. Int J Adv Manuf Technol 131:4345–4357. https://doi.org/10.1007/s00170-024-13241-3
3. Hou H, Zhang P (2025) Lightweight design of industrial robot arm based on thermoplastic carbon fiber reinforced materials. J Phys: Conf Ser 2954:012038. https://doi.org/10.1088/1742-6596/2954/1/012038
4. Hsu CY, Chiang CC, Luo GM, Chen YH, Chu FC (2024) Analysis of Ship Structure with GFRP Lamination Design Subjected to Underwater Shock Loading. Adv Sci Technol 136:23–29. https://doi.org/10.4028/p-aFLx8d
5. Suwarta P, Wisnom MR, Fotouhi M, Wu X, Czél G (2025) Pseudo-ductile compressive behaviour of unidirectional thin-ply carbon /glass fibre-epoxy hybrid composites. Compos Part A: Appl Sci Manufac 195:108877. https://doi.org/10.1016/j.compositesa.2025.108877
6. Liu X, Huang K, Han X, Liang D, Wang X, Zhang L et al (2025) Temperature effect on the fatigue properties of CFRP bolted joints by combining DIC, AE and IRT techniques. Thin-Walled Struct 215:113522. https://doi.org/10.1016/j.tws.2025.113522
7. Geier N, Szalay T, Takács M (2018) Analysis of thrust force and characteristics of uncut fibres at non-conventional oriented drilling of unidirectional carbon fibre-reinforced plastic (UD-CFRP) composite laminates. Int J Adv Manuf Technol 100:3139–3154. https://doi.org/10.1007/s00170-018-2895-8
8. Li Y, Feng Z, Huang L, Essa K, Bilotti E, Zhang H et al (2019) Additive manufacturing high performance graphene-based composites: A review. Compos Part A: Appl Sci Manufac 124:105483. https://doi.org/10.1016/j.compositesa.2019.105483
9. Geier N, Xu J, Poór DI, Dege JH, Davim JP (2023) A review on advanced cutting tools and technologies for edge trimming of carbon fibre reinforced polymer (CFRP) composites. Compos Part B: Eng 266:111037. https://doi.org/10.1016/j.compositesb.2023.111037
10. Li H, Qin X, He G, Jin Y, Sun D, Price M (2016) Investigation of chip formation and fracture toughness in orthogonal cutting of UD-CFRP. Int J Adv Manuf Technol 82:1079–1088. https://doi.org/10.1007/s00170-015-7471-x
11. Geier N, Magyar G (2025) Machining-induced burr distribution along hole contours in unidirectional carbon fibre-reinforced polymer (UD-CFRP) composites. Compos Part C: Open Access 18:100640. https://doi.org/10.1016/j.jcomc.2025.100640
12. Lukács T, Pereszlai C, Geier N (2023) Delamination measurement in glass fibre reinforced polymer (GFRP) composite based on image differencing. Compos Part B: Eng 248:110381. https://doi.org/10.1016/j.compositesb.2022.110381
13. Sakai M, Matsuyama R, Miyajima T (2000) The pull-out and failure of a fiber bundle in a carbon fiber reinforced carbon matrix composite. Carbon 38:2123–2131. https://doi.org/10.1016/S0008-6223(00)00067-1
14. Duboust N, Watson M, Marshall M, O'Donnel GE, Kerrigan K (2021) Towards intelligent CFRP composite machining: Surface analysis methods and statistical data analysis of machined fibre laminate surfaces. Proc Institution Mech Eng Part B: J Eng Manuf 235:1602–1617. https://doi.org/10.1177/0954405420960920
15. Ashworth S, Fairclough J, Monoranu M, Ghadbeigi H, Meredith J, Takikawa Y et al (2020) Epifluorescent microscopy of edge-trimmed carbon fibre-reinforced polymers: An alternative to computed tomography scanning. Adv Compos Lett 29:2633366X20924676. https://doi.org/10.1177/2633366X20924676
16. Geng D, Liu Y, Shao Z, Lu Z, Cai J, Li X et al (2019) Delamination formation, evaluation and suppression during drilling of composite laminates: A review. Compos Struct 216:168–186. https://doi.org/10.1016/j.compstruct.2019.02.099
17. Pereszlai C, Geier N (2020) A comparative analysis of wobble milling, helical milling and conventional drilling of CFRP. Int J

Adv Manuf Technol 106:3913–3930. https://doi.org/10.1007/s00170-019-04842-4
18. Shunmugesh K, Paul B, Sarker B, Chakraborty S (2025) Parametric study and multi-objective optimization of milling of CFRP composite laminates. Int J Interact Des Manuf 19:5239–5254. https://doi.org/10.1007/s12008-024-02130-4
19. Geier N, Szalay T, Biró I (2018) Trochoid milling of carbon fibre-reinforced plastics (CFRP). Procedia CIRP 77:375–378. https://doi.org/10.1016/j.procir.2018.09.039
20. Hintze W, Brügmann F (2018) Influence of spatial tool inclination on delamination when milling CFRP. J Mater Process Technol 252:830–837. https://doi.org/10.1016/j.jmatprotec.2017.10.041
21. Jia Z, Fu R, Niu B, Qian B, Bai Y, Wang F (2016) Novel drill structure for damage reduction in drilling CFRP composites. Int J Mach Tools Manuf 110:55–65. https://doi.org/10.1016/j.ijmachtools.2016.08.006
22. Hosokawa A, Hirose N, Ueda T, Furumoto T (2014) High-quality machining of CFRP with high helix end mill. CIRP Ann 63:89–92. https://doi.org/10.1016/j.cirp.2014.03.084
23. Pascual V, San-Juan M, Santos FJ, Martín Ó, de Tiedra MP (2017) Study of axial cutting forces and delamination phenomenon in drilling of carbon fiber composites. Procedia Manuf 13:67–72. https://doi.org/10.1016/j.promfg.2017.09.010
24. Voss R, Seeholzer L, Kuster F, Wegener K (2017) Influence of fibre orientation, tool geometry and process parameters on surface quality in milling of CFRP. CIRP J Manufact Sci Technol 18:75–91. https://doi.org/10.1016/j.cirpj.2016.10.002
25. Hintze W, Hartmann D, Schütte C (2011) Occurrence and propagation of delamination during the machining of carbon fibre reinforced plastics (CFRPs) – An experimental study. Compos Sci Technol 71:1719–1726. https://doi.org/10.1016/j.compscitech.2011.08.002
26. Wang F, Yin J, Ma J, Jia Z, Yang F, Niu B (2017) Effects of cutting edge radius and fiber cutting angle on the cutting-induced surface damage in machining of unidirectional CFRP composite laminates. Int J Adv Manuf Technol 91:3107–3120. https://doi.org/10.1007/s00170-017-0023-9
27. Navarro-Mas MD, García-Manrique JA, Meseguer MD, Ordeig I, Sánchez AI (2018) Delamination Study in Edge Trimming of Basalt Fiber Reinforced Plastics (BFRP). Materials 11:1418. https://doi.org/10.3390/ma11081418
28. Ahmad JS, Shahid AH (2013) Effect of edge trimming on failure stress of carbon fibre polymer composites. IJMMM 13:331. https://doi.org/10.1504/IJMMM.2013.053231
29. Ahmad J (2009) Machining of polymer composites. Springer US
30. Kim J, Kim Y-B, Seo JW, Park HW (2019) Deburring drilled holes in CFRP composites with large pulsed electron beam (LPEB) irradiation. J Manuf Process 40:68–75. https://doi.org/10.1016/j.jmapro.2019.03.001
31. Li M, Huang M, Jiang X, Kuo C, Yang X (2018) Study on burr occurrence and surface integrity during slot milling of multidirectional and plain woven CFRPs. Int J Adv Manuf Technol 97:163–173. https://doi.org/10.1007/s00170-018-1937-6
32. Geier N, Poór DI, Pereszlai C, Tamás-Bényei P (2022) Drilling of recycled carbon fibre–reinforced polymer (rCFRP) composites: analysis of burrs and microstructure. Int J Adv Manuf Technol. https://doi.org/10.1007/s00170-022-08847-4
33. Hintze W, Cordes M, Koerkel G (2015) Influence of weave structure on delamination when milling CFRP. J Mater Process Technol 216:199–205. https://doi.org/10.1016/j.jmatprotec.2014.09.004
34. Sheikh-Ahmad JY, Dhuttargaon M, Cheraghi H (2017) New tool life criterion for delamination free milling of CFRP. Int J Adv Manuf Technol 92:2131–2143. https://doi.org/10.1007/s00170-017-0240-2
35. Janardhan P, Sheikh-Ahmad J, Cheraghi H (2006) Edge trimming of CFRP with diamond interlocking tools. 2006–2001. https://doi.org/10.4271/2006-01-3173
36. Ramulu M, Colligan K (2008) Edge finishing and delamination effects induced during abrasive waterjet machining on the compression strength of a graphite/epoxy composite, American society of mechanical engineers digital collection 173–179. https://doi.org/10.1115/IMECE2005-82346
37. Sheikh-Ahmad J, Urban N, Cheraghi H (2012) Machining Damage in Edge Trimming of CFRP. Mater Manuf Processes 27:802–808. https://doi.org/10.1080/10426914.2011.648253
38. Khashaba UA (2022) A novel approach for characterization of delamination and burr areas in drilling FRP composites. Compos Struct 290:115534. https://doi.org/10.1016/j.compstruct.2022.115534
39. Babu J, Sunny T, Bhullar JP (2016) A Digital Image Analysis to Evaluate Delamination Factor after Drilling GFRP Composites using a Kevlar Drill Bit. INDJST 9:1–7. https://doi.org/10.17485/ijst/2016/v9iS1/85749
40. Wang F, Yin J, Jia Z, Niu B, Liu W (2018) A novel approach to evaluate the delamination extent after edge trimming of carbon-fiber-reinforced composites. Proc Institution Mech Eng Part B: J Eng Manuf 232:2523–2532. https://doi.org/10.1177/0954405417699015
41. Lowe DG (2004) Distinctive Image Features from Scale-Invariant Keypoints. Int J Comput Vision 60:91–110. https://doi.org/10.1023/B:VISI.0000029664.99615.94